Supporting Information for "Jupiter's Temperate Belt/Zone Contrasts Revealed at Depth by Juno Microwave Observations"

L.N. Fletcher[1], F.A. Oyafuso[2], M. Allison[3], A. Ingersoll[4], L. Li[5], Y. Kaspi[6], E. Galanti[6], M.H. Wong[7], G.S. Orton[2], K. Duer[6], Z. Zhang[4], C. Li[8], T. Guillot[9], S.M. Levin[2], S. Bolton[10]

[1]School of Physics and Astronomy, University of Leicester, University Road, Leicester, LE1 7RH, UK

[2]Jet Propulsion Laboratory, California Institute of Technology, 4800 Oak Grove Drive, Pasadena, CA 91109, USA

[4]California Institute of Technology, Pasadena, CA, USA

[3]Goddard Institute for Space Studies, New York, NY, USA

[5]University of Houston, Houston, TX, USA

[6]Department of Earth and Planetary Sciences, Weizmann Institute of Science, Rehovot 76100, Israel

[7]SETI Institute, Mountain View, CA, 94043-5139, USA

[8]University of Michigan, Ann Arbor, MI, USA.

[9]Universitié Côte d'Azur, OCA, Lagrange CNRS, 06304 Nice, France

[10]Southwest Research Institute, San Antonio, Texas, TX, USA.

Contents of this file

1. Text S1 to S4

2. Figures S1 to S8

3. Tables S1 to S2

Introduction

This document includes supporting text and figures for Juno microwave observations of Jupiter's belt/zone structure, and the finding that Jupiter's belts switch from being microwave-bright (i.e., ammonia depleted and/or physically warm) in the upper troposphere to being microwave-dark (i.e., ammonia enriched and/or physically cool) in the deeper troposphere, with a transition level (which we call the jovicline) occurring in the 4-10 bar range. This supporting information contains alternative figures and experiments mentioned in the main text.

Text S1. Cassini Winds vs. Hubble Winds

The main article uses cloud-top zonal winds derived from Cassini/ISS measurements (Porco et al., 2003) during the 2000 Jupiter flyby. In particular, Fig. 4 showcases the strength of the Pearson and Spearman correlation between the microwave brightness gradients (Δ) and the cloud-top winds, showing how the results fall naturally into two groups: positive correlation in deep-sounding channels 1-3 (11.5-50 cm), and negative correlation in shallow-sounding channels 4-6 (1.4-5.75 cm). In Figs. S1 and S2 we instead use cloud-top winds derived in 2017 (Tollefson et al., 2017) and 2019 (Wong et al., 2020) from Hubble Space Telescope WFC3 observations. Although the zonal winds have remained rather stable over time, small changes in the windspeeds do occur, and can have a small effect on the strength of the correlations. The Pearson correlation coefficients for each hemisphere, wavelength, and zonal wind profile are compared in Table S1, where we find small improvements in the strength of the positive and negative correlations when the Hubble winds are used, but no alteration to the conclusions of our study in the main article. For completeness, Table S2 also provides the p-values for each correlation, with values significantly smaller than 0.05 allowing us to firmly reject the null hypothesis that the winds and the MWR gradients are uncorrelated. The p-values only come close to this limit in Channels 4 (southern hemisphere) and 3 (northern hemisphere) where the correlation coefficient tends to zero near the jovicline.

Text S2. Robustness of Correlations

The main text uses a weighted average over nine perijoves of the coefficients used to define the limb darkening observed by MWR in each channel, using the techniques of Oyafuso et al. (2020). Fig. 5 of the main text shows the variation with emission angle of the Pearson correlation coefficient r_{xy} between cloud-tracked winds from Cassini and microwave brightness gradients. Fig. S3 shows the how the corresponding p_{xy} values vary with emission angle, confirming that the null hypothesis (that winds and microwave gradients are uncorrelated) can be rejected everywhere except in MWR channel 3 for emission angles of $\sim 45°$ in the north and $\sim 75°$ in the south. These are the transition points, where the correlation flips from positive to negative, and are assigned to the 5-14 bar range in the main text.

We can also question whether the measured pseudoshears and correlations can change if we use different combinations of perijoves, rather than all nine. In this section, we explore the robustness of the correlations. From nine different perijoves there are 36 different combinations of two perijoves. For each of these 36 pairs, we compute the mean nadir brightness temperature and the associated pseudo-windshear Δ, shown as the scatter of points at each latitude in Fig. S4. The same basic structure of peaks in Δ coinciding with peaks in the cloud-tracked winds persists for all 36 combinations, although the scatter becomes larger for the deep-sounding channels 1 and 2 (24-50 cm). This is consistent with the fact that Ingersoll et al. (2017) were able to identify the switch in the brightness of the belts even from a single perijove (PJ1).

Next, we recompute the Pearson and Spearman correlation coefficients for each of the 36 combinations in Fig. S5, along with the associated probability values in Fig. S6. Each

pair of perijoves confirms that the correlation between Δ and the cloud-tracked winds falls into two distinct categories (negative correlation for shallow-sounding channels, positive correlation in deep-sounding channels), and show that correlation is weak in the southern hemisphere for Channel 4, and weak in the northern hemisphere for Channel 3. The strength of the correlation does change depending on which PJ pairs are considered, which is why the main article uses a weighted average over all nine. The p-values reveal a similar story - if the p-value is considerably smaller than 0.05 (the topmost dotted horizontal line), then the correlation is statistically significant and we can firmly reject the null hypothesis of zero correlation between the MWR Δ and the winds. This is the case for shallow-sounding channels 5 and 6, and for deep-sounding channels 2 and 3 in the south. Fig. S6 also confirms that zero correlation is found in channel 4 (south) and channel 3 (north), where the transition is occurring. However, we find that channel 1 p-values in some PJ pairs are sufficiently large that we cannot reject the null hypothesis (some exceeding $p = 0.05$). This implies that, if we only had observations from two perijoves, the correlation in channel 1 would be hard to see, again consistent with Ingersoll et al. (2017), who could see the correlation in the 40-60 bar range with PJ1 data, but not deeper. We conclude that the detection of the correlation with statistical significance at the deepest levels sensed by MWR is only made possible via the weighted average of more than two perijoves.

Text S3. Alternative Contribution Functions

In the main text, we point out that the depths sounded by each MWR channel can only be estimated using a model - specifically, the vertical distribution of gases like ammonia and water, and models for their spectral opacity. In the main article we use the current best estimates of the latitudinal distribution of NH_3 (Guillot et al., 2020) to calculate contribution functions to assign pressure ranges to each MWR channel. As a demonstration of model dependence, Fig. S7 recomputes these contribution functions using a more simplistic NH_3 distribution. Namely, we assume NH_3 to be uniform in latitude, to have a deep abundance equivalent to 2.76× the solar NH_3 abundance (Li et al., 2017), and to decrease with altitude as it condenses into cloud decks assuming thermochemical equilibrium. These assumptions are typically used to report the altitude sensitivity of MWR (Janssen et al., 2017), and a comparison of Fig. S7 with Fig. 6 of our main article shows how the peak pressure levels change. Specifically, the depth sounded at nadir changes from $\sim$ 5 bar to $\sim$ 3.6 bar in Channel 4, and from $\sim$ 14 bar to $\sim$ 9.5 bar in Channel 3, if we use the crude NH_3 vertical distribution, which would have the effect of moving the transition level to slightly shallower pressures. Sharp kinks in the contribution occur where NH_3, NH_4SH and H_2O condense with these assumptions. We expect the contribution functions reported in the main article to be a more accurate representation of the altitude sensitivity, given that they incorporate the measured NH_3 depletion down to the 40-60 bar level (Li et al., 2017).

Text S4. Calculation of Gravity and Height

In order to integrate the thermal wind equation as a function of altitude, and to adjust for gravitational acceleration in our measurement of microwave brightness gradients, we must match our pressure grid to an appropriate altitude grid $z(\phi, p)$ and gravitational acceleration $g(\phi, p)$. Fig. S8 shows our two grids, calculated using the gravitational and centrifugal potential of Buccino, Helled, Parisi, Hubbard, and Folkner (2020) and the ideal gas law, cross-checking the estimated heights with those measured by the Galileo probe (Seiff et al., 1998).

References

Bellotti, A., Steffes, P. G., & Chinsomboom, G. (2016, December). Laboratory measurements of the 5-20 cm wavelength opacity of ammonia, water vapor, and methane under simulated conditions for the deep jovian atmosphere. *Icarus*, *280*, 255-267. doi: 10.1016/j.icarus.2016.07.013

Buccino, D. R., Helled, R., Parisi, M., Hubbard, W. B., & Folkner, W. M. (2020, August). Updated Equipotential Shapes of Jupiter and Saturn Using Juno and Cassini Grand Finale Gravity Science Measurements. *Journal of Geophysical Research (Planets)*, *125*(8), e06354. doi: 10.1029/2019JE006354

Guillot, T., Li, C., Bolton, S. J., Brown, S. T., Ingersoll, A. P., Janssen, M. A., ... Stevenson, D. J. (2020, August). Storms and the Depletion of Ammonia in Jupiter: II. Explaining the Juno Observations. *Journal of Geophysical Research (Planets)*, *125*(8), e06404. doi: 10.1029/2020JE006404

Hanley, T. R., Steffes, P. G., & Karpowicz, B. M. (2009, July). A new model of the hydrogen and helium-broadened microwave opacity of ammonia based on extensive

laboratory measurements. *Icarus*, *202*, 316-335. doi: 10.1016/j.icarus.2009.02.002

Ingersoll, A. P., Adumitroaie, V., Allison, M. D., Atreya, S., Bellotti, A. A., Bolton, S. J., ... Steffes, P. G. (2017, August). Implications of the ammonia distribution on Jupiter from 1 to 100 bars as measured by the Juno microwave radiometer. *Geophys. Res. Lett.*, *44*, 7676-7685. doi: 10.1002/2017GL074277

Janssen, M. A., Oswald, J. E., Brown, S. T., Gulkis, S., Levin, S. M., Bolton, S. J., ... Wang, C. C. (2017, November). MWR: Microwave Radiometer for the Juno Mission to Jupiter. *Space Sci. Rev.*, *213*, 139-185. doi: 10.1007/s11214-017-0349-5

Li, C., Ingersoll, A., Janssen, M., Levin, S., Bolton, S., Adumitroaie, V., ... Williamson, R. (2017, June). The distribution of ammonia on Jupiter from a preliminary inversion of Juno microwave radiometer data. *Geophys. Res. Lett.*, *44*, 5317-5325. doi: 10 .1002/2017GL073159

Oyafuso, F., Levin, S., Orton, G., Brown, S. T., Adumitroaie, V., Janssen, M., ... Bolton, S. (2020, November). Angular Dependence and Spatial Distribution of Jupiter's Centimeter-Wave Thermal Emission From Juno's Microwave Radiometer. *Earth and Space Science*, *7*(11), e01254. doi: 10.1029/2020EA001254

Porco, C. C., West, R. A., McEwen, A., Del Genio, A. D., Ingersoll, A. P., Thomas, P., ... Vasavada, A. R. (2003, March). Cassini Imaging of Jupiter's Atmosphere, Satellites, and Rings. *Science*, *299*, 1541-1547. doi: 10.1126/science.1079462

Seiff, A., Kirk, D. B., Knight, T. C. D., Young, R. E., Mihalov, J. D., Young, L. A., ... Atkinson, D. (1998, September). Thermal structure of Jupiter's atmosphere near the edge of a 5-μm hot spot in the north equatorial belt. *J. Geophys. Res.*, *103*, 22857-22890. doi: 10.1029/98JE01766

Tollefson, J., Wong, M. H., Pater, I. d., Simon, A. A., Orton, G. S., Rogers, J. H., ... Marcus, P. S. (2017, November). Changes in Jupiter's Zonal Wind Profile preceding and during the Juno mission. *Icarus*, *296*, 163-178. doi: 10.1016/j.icarus.2017.06.007

Wong, M. H., Simon, A. A., Tollefson, J. W., de Pater, I., Barnett, M. N., Hsu, A. I., ... Fletcher, L. N. (2020, April). High-resolution UV/Optical/IR Imaging of Jupiter in 2016-2019. *ApJ Supplement*, *247*(2), 58. doi: 10.3847/1538-4365/ab775f

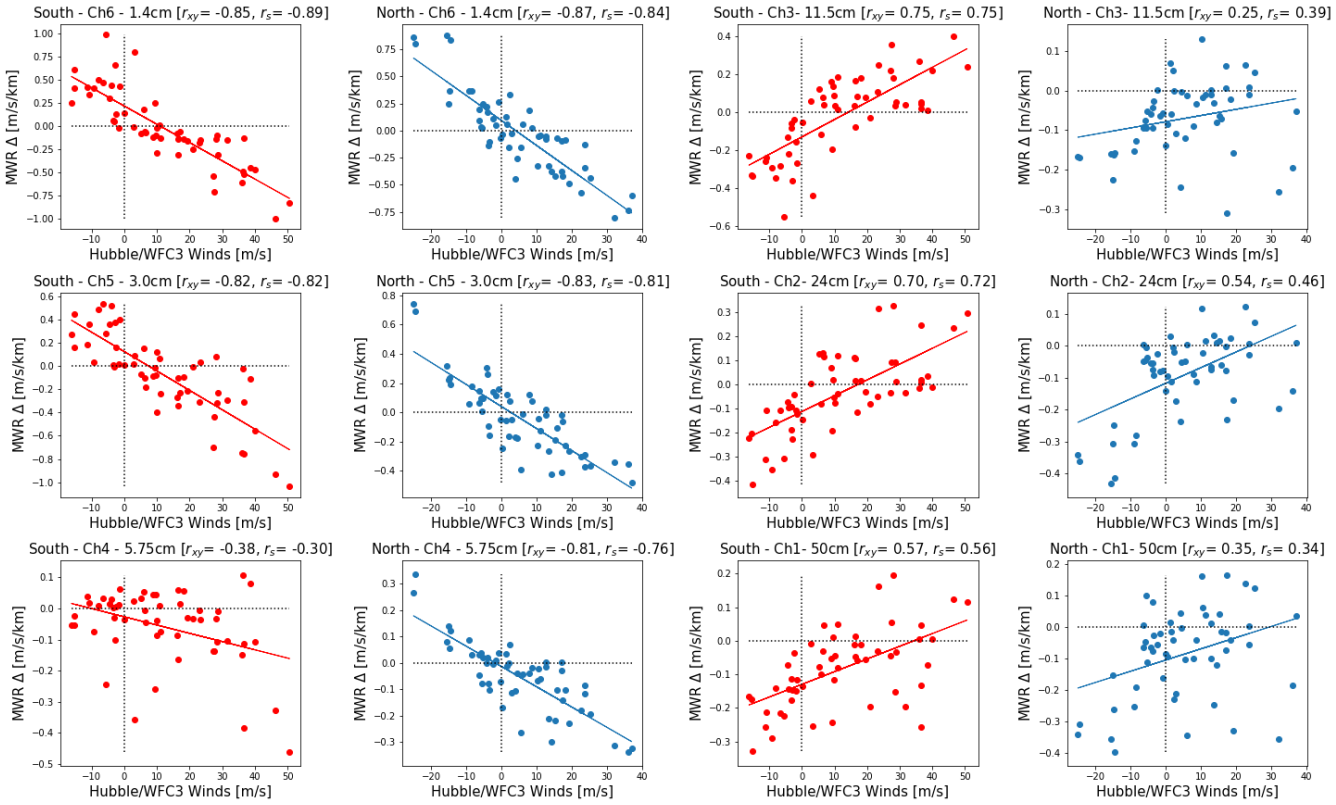

Figure S1. Scatter plots revealing negative (channels 4-6, left columns) and positive (channels 1-3, right columns) correlations between the nadir microwave T_B gradients Δ and the Hubble cloud-tracked winds of Tollefson et al. (2017) for February 2017. Only latitudes between 25° and 65° in each hemisphere are included. Southern-hemisphere correlations are in red, northern-hemisphere correlations are in blue. A linear trend line has been added as a guide. The Pearson r_{xy} and Spearman's ranked r_s correlation coefficients are provided for each channel and hemisphere.

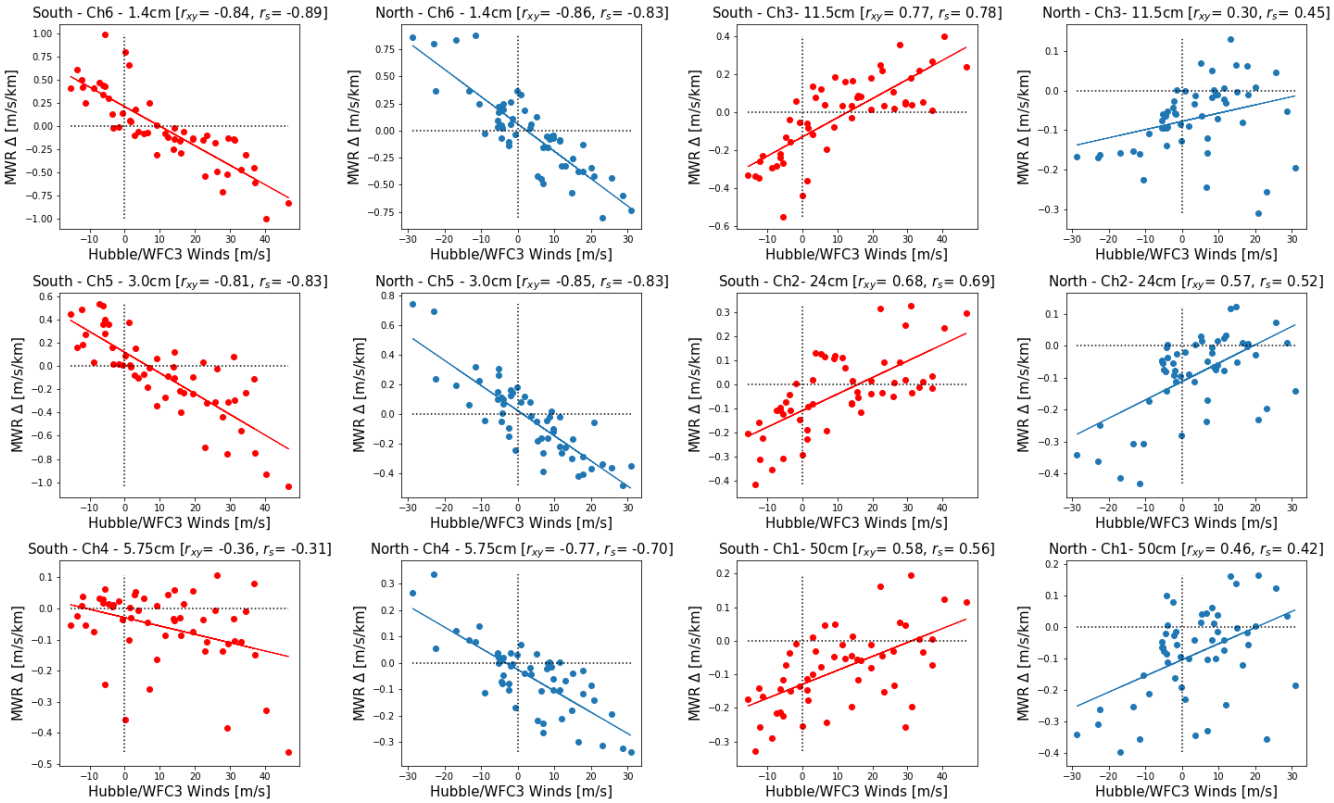

Figure S2. Scatter plots revealing negative (channels 4-6, left columns) and positive (channels 1-3, right columns) correlations between the nadir microwave T_B gradients Δ and the Hubble cloud-tracked winds of Wong et al. (2020) for June 2019. Only latitudes between 25° and 65° in each hemisphere are included. Southern-hemisphere correlations are in red, northern-hemisphere correlations are in blue. A linear trend line has been added as a guide. The Pearson r_{xy} and Spearman's ranked r_s correlation coefficients are provided for each channel and hemisphere.

Table S1. Comparing Pearson correlation coefficients between nadir microwave brightness gradients Δ and cloud-top zonal winds from Cassini in 2000 (Porco et al., 2003) and Hubble in 2017 (Tollefson et al., 2017) and 2019 (Wong et al., 2020).

Channel	Wavelength (cm)	Cassini-2000 r_{xy}	Hubble-2017 r_{xy}	Hubble-2019 r_{xy}
South				
1	50	0.545	0.566	0.581
2	24	0.673	0.697	0.680
3	11.5	0.754	0.754	0.775
4	5.75	-0.271	-0.382	-0.361
5	3.0	-0.741	-0.816	-0.813
6	1.4	-0.820	-0.847	-0.845
North				
1	50	0.455	0.351	0.459
2	24	0.559	0.539	0.575
3	11.5	0.340	0.249	0.300
4	5.75	-0.720	-0.808	-0.771
5	3.0	-0.814	-0.831	-0.850
6	1.4	-0.821	-0.866	-0.861

Table S2. Comparing Pearson correlation p-values between nadir microwave brightness gradients Δ and cloud-top zonal winds from Cassini in 2000 (Porco et al., 2003) and Hubble in 2017 (Tollefson et al., 2017) and 2019 (Wong et al., 2020).

Channel	Wavelength (cm)	Cassini-2000 p_{xy}	Hubble-2017 p_{xy}	Hubble-2019 p_{xy}
South				
1	50	2.06×10^{-05}	8.21×10^{-06}	4.11×10^{-06}
2	24	2.46×10^{-08}	4.67×10^{-09}	1.54×10^{-08}
3	11.5	4.70×10^{-11}	4.52×10^{-11}	6.14×10^{-12}
4	5.75	4.72×10^{-02}	4.35×10^{-03}	7.40×10^{-03}
5	3.0	1.47×10^{-10}	5.97×10^{-14}	8.54×10^{-14}
6	1.4	3.33×10^{-14}	6.7×10^{-16}	9.85×10^{-16}
North				
1	50	5.52×10^{-04}	9.33×10^{-03}	4.87×10^{-04}
2	24	1.12×10^{-05}	2.58×10^{-05}	5.49×10^{-06}
3	11.5	1.19×10^{-02}	6.96×10^{-02}	2.76×10^{-02}
4	5.75	8.32×10^{-10}	1.53×10^{-13}	9.46×10^{-12}
5	3.0	7.07×10^{-14}	7.79×10^{-15}	4.10×10^{-16}
6	1.4	2.79×10^{-14}	2.76×10^{-17}	7.20×10^{-17}

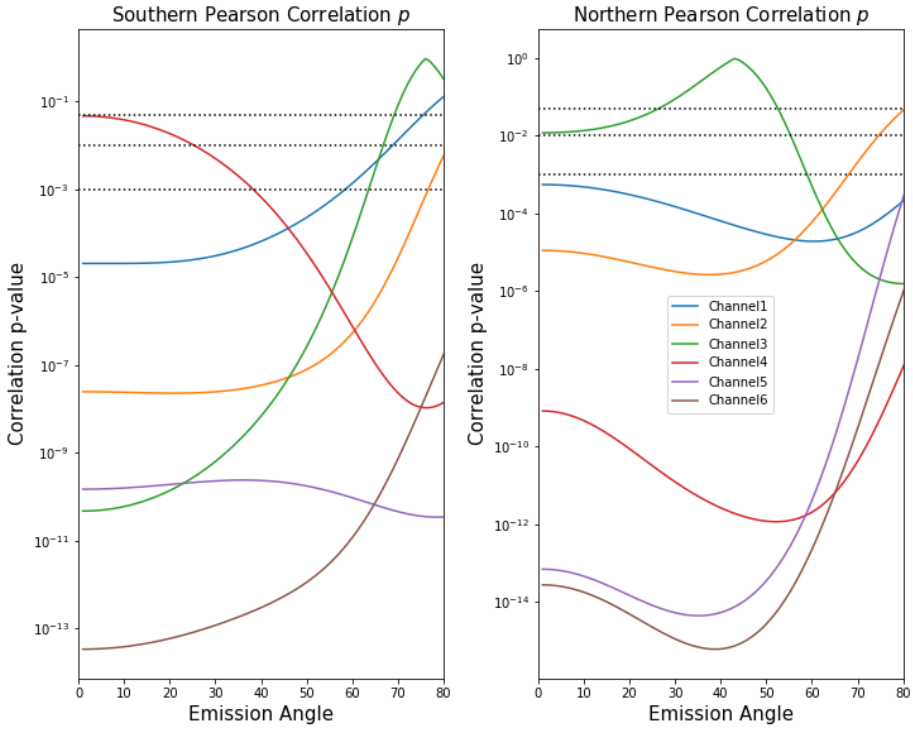

Figure S3. Variation of the p_{xy} values with emission angle for the Pearson correlation coefficients r_{xy} between Cassini winds and MWR brightness gradients shown in Fig. 5 of the main text. Horizontal lines at 0.05, 0.01 and 0.001 show the thresholds for statistical significance (values below 0.05 allowing rejection of the null hypothesis that the winds and MWR brightnesses are uncorrelated).

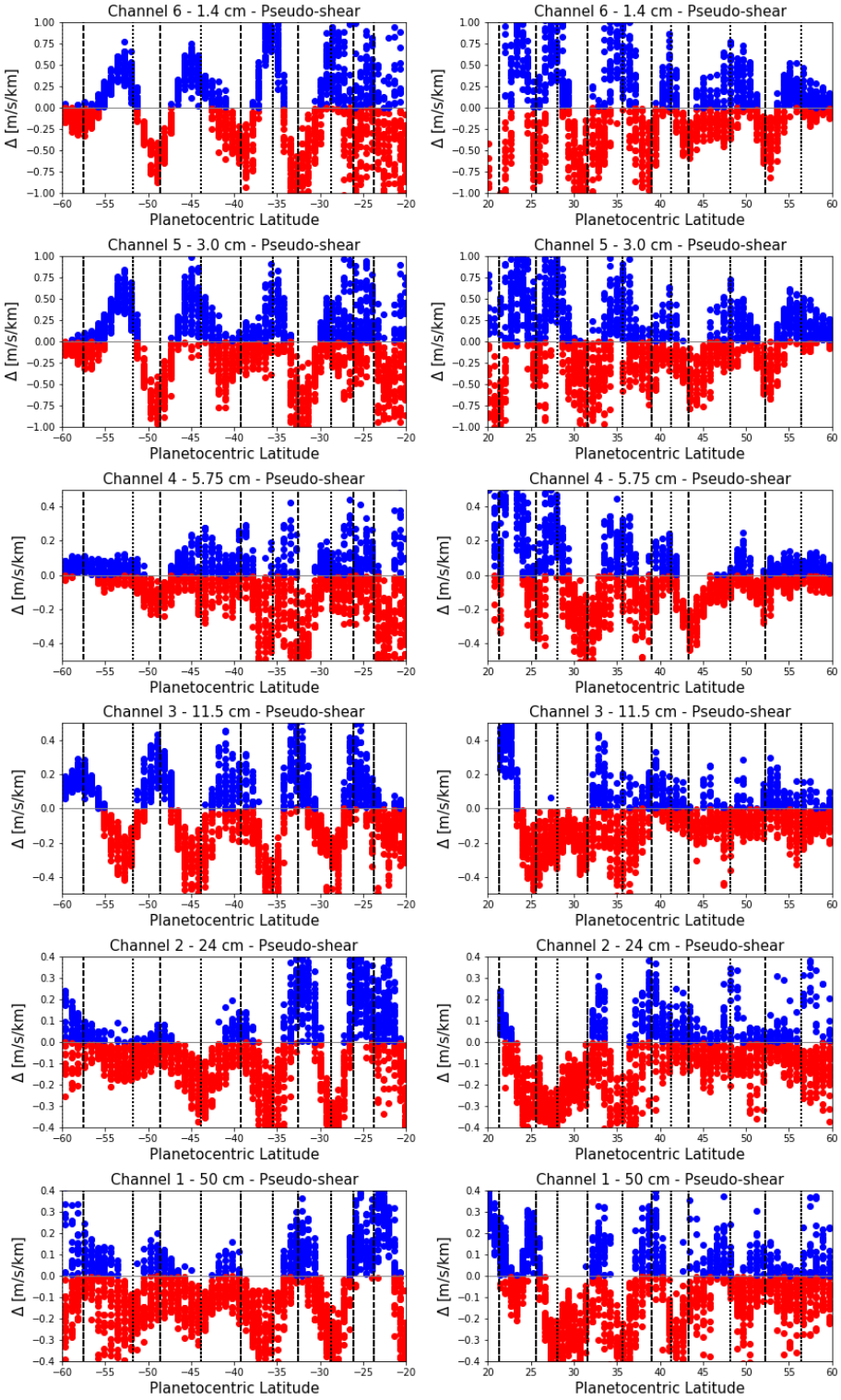

Figure S4. Assessing the robustness of the MWR brightness temperature gradients from the main paper, where a weighted average of the nadir c_0 coefficient over nine perijoves was used to compute Δ. Here we take 36 combinations of two perijoves from the nine, and recompute Δ for each pair.

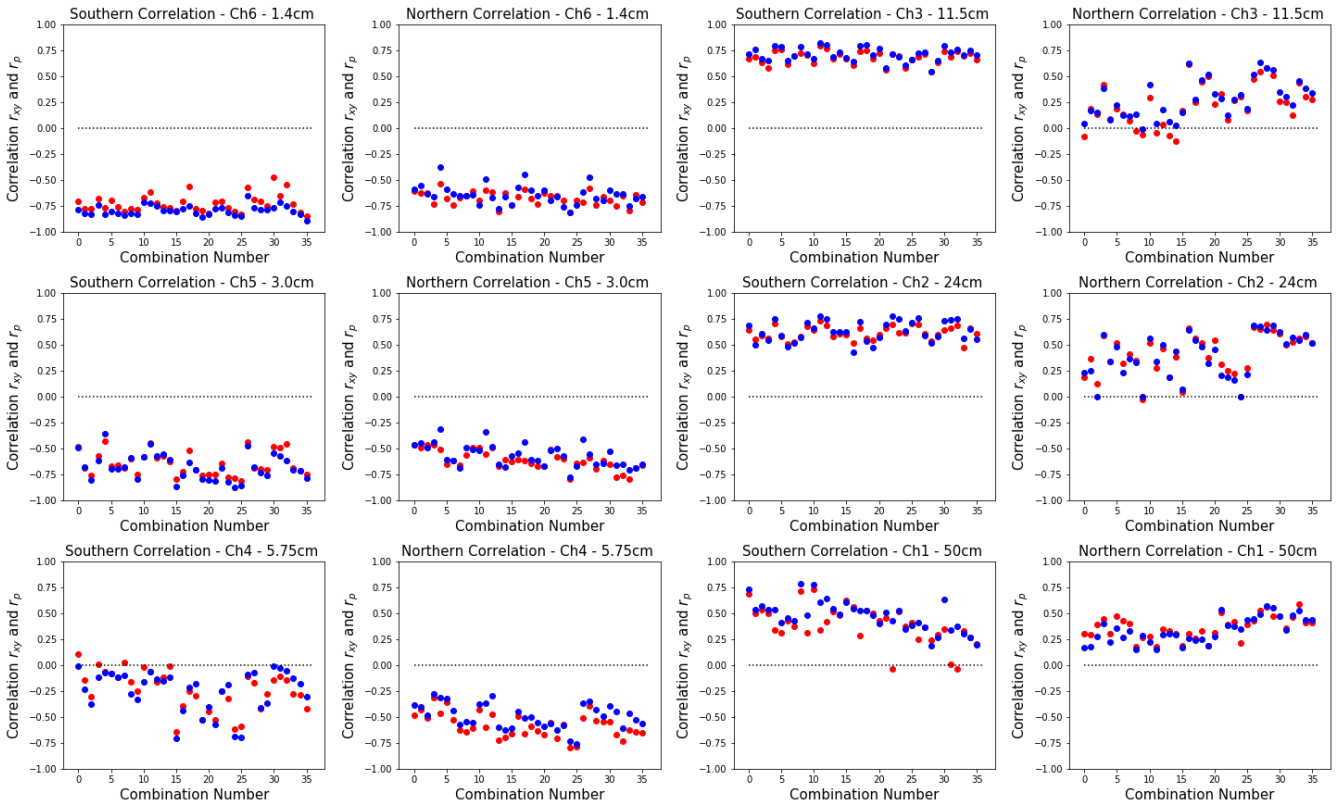

Figure S5. The Pearson and Spearman correlation coefficients (red and blue, respectively) for each of the 36 pairs of perijoves, confirming that the correlations identified in the main article from a weighted average of nine perijoves are robust.

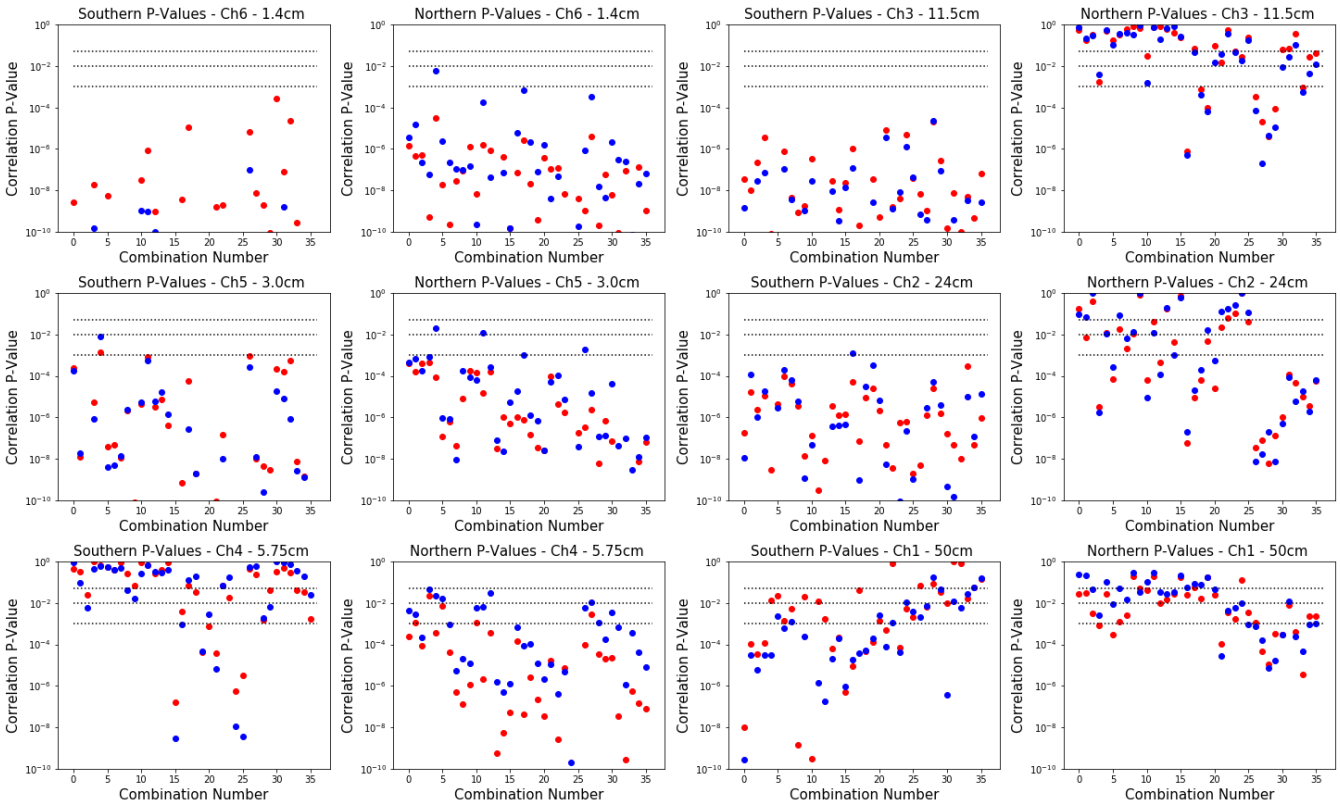

Figure S6. Probability values for the Pearson and Spearman correlation coefficients (red and blue, respectively) for each of the 36 pairs of perijoves in Fig. S5. Any dot falling below the topmost horizontal line at 0.05 is considered to be statistically significant, dots falling below the lower horizontal line at 0.001 is considered highly statistically significant.

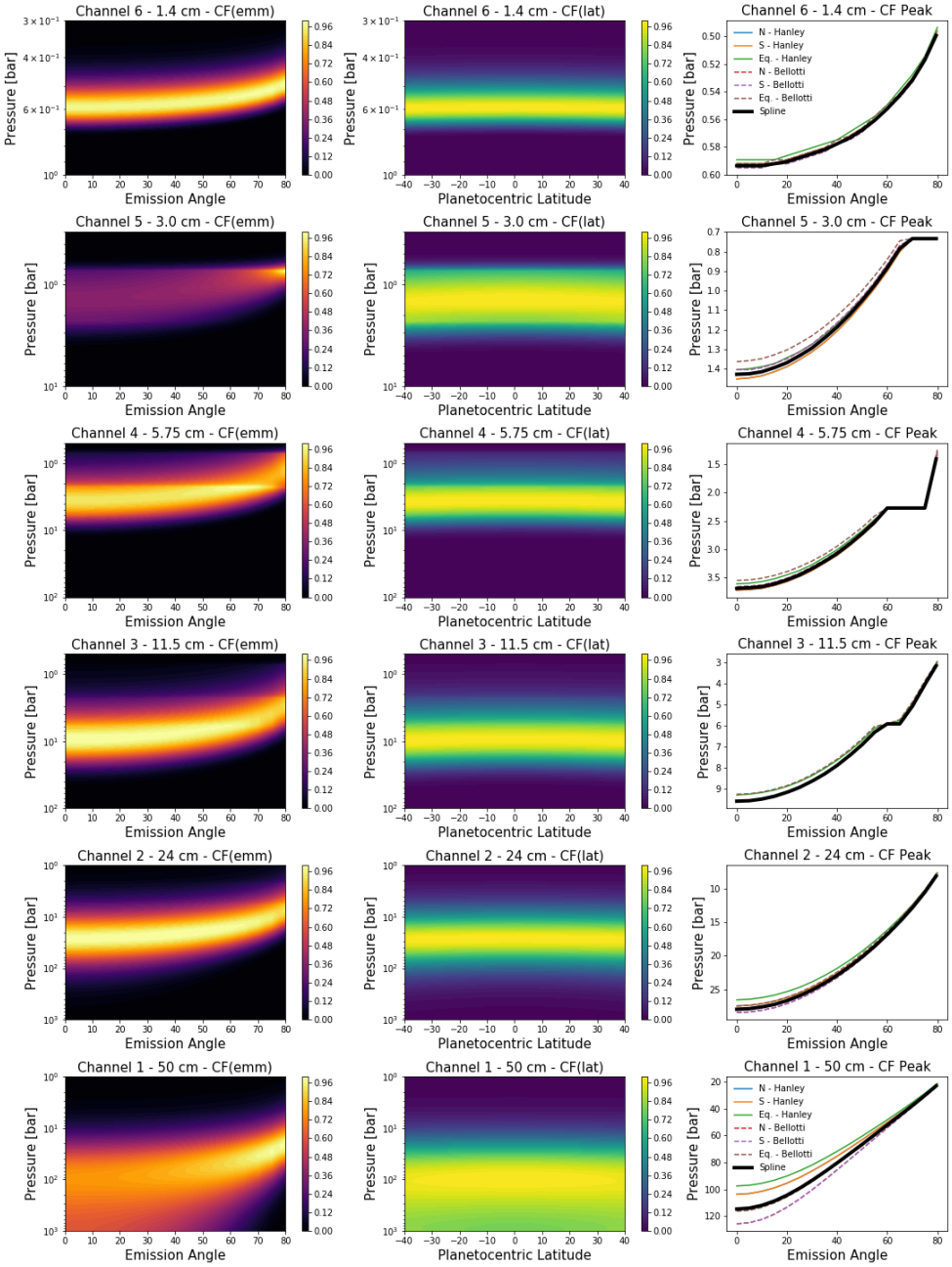

Figure S7. Contribution functions based on a deep 2.76× enrichment of NH_3, decreasing with height as the different cloud layers condense. Left: normalised contribution functions as a function of emission angle for the equator. Centre: normalised contribution functions at zero emission angle (nadir view) for all latitudes. Right: peak pressure of the contribution function averaged over three regions (north 20°N to 40°N; south 20°S to 40°S; and equator 5°N to 5°S) using two different NH_3 opacity models - Hanley et al. (2009) as the solid lines and Bellotti et al. (2016) as the dashed lines. The solid black line is the spline-interpolated contribution function described in the main text.

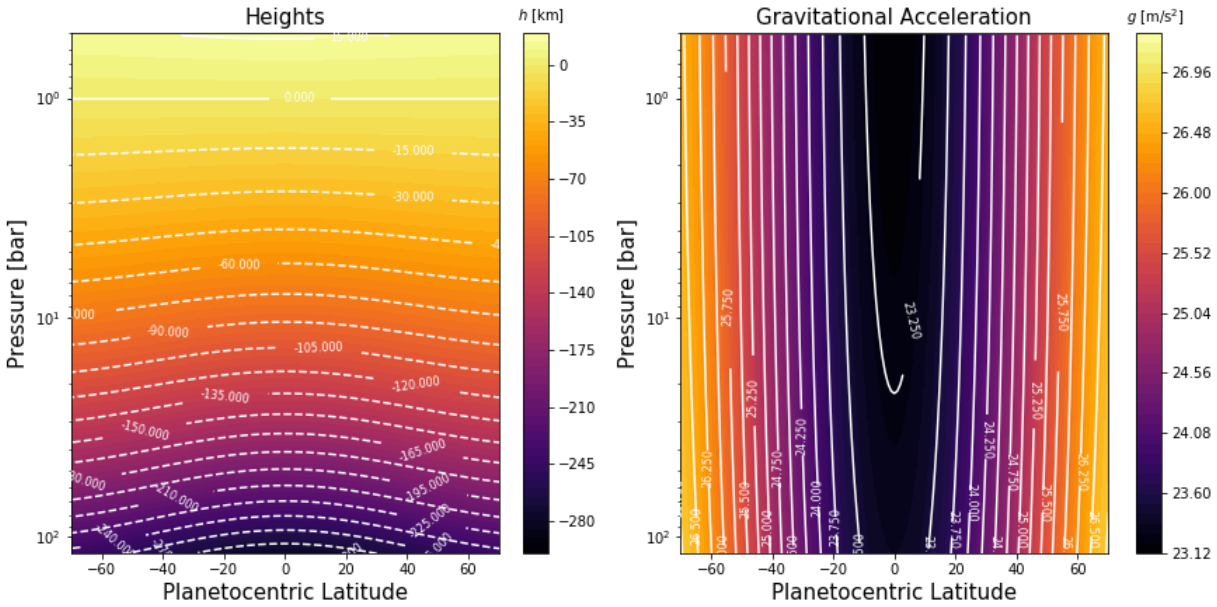

Figure S8. Estimates of Jupiter's height and gravitational acceleration for use in the estimates of pseudo-shears and integrated zonal winds. We used the combined gravitational and centrifugal potential of Buccino et al. (2020) to estimate the effective gravity $g(\phi, p)$, reproducing their 1-bar gravitational acceleration. The ideal gas law then allows us to calculate the depths $z(\phi, p)$, which matches those measured by the Galileo probe (Seiff et al., 1998).